Role of lithium codoping in enhancing the scintillation yield of aluminate garnets

Yuntao Wu,*[,a] Ge Yang,[b] Dan Han,[c,d,e] Ming Liu,[b] Ayman Hawari,[b] Mao-Hua Du,*[,c] Jing Peng,[f] Camera Foster,[g,h] Shiyou Chen,[d,e] Merry Koschan,[g] Charles L. Melcher [g,h,i,j]

[a] *Artificial Crystal Research Center, Shanghai Institute of Ceramics, Chinese Academy of Sciences, Shanghai, 201800, China*

[b] *Department of Nuclear Engineering, North Carolina State University, Raleigh, NC 27695, USA*

[c] *Materials Science and Technology Division, Oak Ridge National Laboratory, Oak Ridge, TN 37831, USA*

[d] *Key Laboratory of Polar Materials and Devices (Ministry of Education) and* [e] *Department of Physics, East China Normal University, Shanghai 200241, China*

[f] *School of Materials Science & Engineering, Beihang University, Beijing 100191, China*

[g] *Scintillation Materials Research Center, University of Tennessee, Knoxville, Tennessee 37996, USA*

[h] *Department of Materials Science and Engineering, University of Tennessee, Knoxville, Tennessee 37996, USA*

[i] *Department of Nuclear Engineering, University of Tennessee, Knoxville, TN 37996, USA*

[j] *Bredesen Center for Interdisciplinary Research and Graduate Education, University of Tennessee, Knoxville, TN 37996, USA*

Abstract The aim of this work is to clarify the scintillation yield enhancement in LuYAG:Pr scintillators obtained by Li co-doping via integrated study of the valence state of activators, the preferential site occupancy of Li co-dopants, and defect structures from experimental and theoretical insights. With Li co-doping, the light yield and

energy resolution of 10×10×10 mm^3 LuYAG:Pr samples are improved from 15,600 to 24,800 photons/MeV, and 5.3 to 4.3% at 662 keV, respectively. The optical absorption spectra indicate that Li co-doping does not induce conversion of stable Pr^{3+} to Pr^{4+} in LuYAG:Pr single crystals. Based on the formation energies of substitutional and interstitial Li sites using density functional theory (DFT) calculations and the ^7Li nuclear magnetic resonance results, it is shown that the Li ions prefer to dominantly occupy the 4-fold coordinated interstitial sites and 4-fold coordinated Al sites. The systematic analysis of thermoluminescence glow curves, positron annihilation lifetime spectroscopies, and defect formation energies derived from DFT calculations reveals that the concentration of isolated Lu and Al vacancies as dominant acceptor defects is reduced by Li codoping, whilst the shallow Li_i interstitial defects and the deep V_O oxygen vacancies are introduced simultaneously. We propose that the lowering of hole trapping at defects resulting from Li co-doping contributes to the scintillation yield enhancement.

Keywords: Inorganic scintillators, garnets, codoping, site occupancy, defect structures

Corresponding author email: ytwu@mail.sic.ac.cn (Y. Wu); mhdu@ornl.gov (M. -H. Du)

I. INTRODUCTION

Inorganic scintillators as important radiation detection materials emit light pulses with wavelengths that are detectable by photosensors in response to ionizing radiation, such as x- and γ-ray, and α- and β- particles. They have been broadly employed in the advanced radiation detectors for oil well logging, high energy physics, nuclear medical imaging, and homeland security applications [1]. Detection efficiency and γ-ray spectral resolution are two critical operation parameters for the nuclear medical imaging and homeland security applications, such as single-photon emission computer tomography (SPECT) and radioisotope identification devices (RIDs). At present, thallium doped sodium iodide (NaI:Tl), discovered in 1948 [2], is still the workhorse for these two applications due to its low cost and sufficient performance. However, in quest of better discrimination of scattered photons for SPECT, and better radionuclide identification capability for RIDs, there is an urgent and realistic need to search for next-generation high-performance scintillation materials.

Over the last two decades, much work has been focused on developing high-energy-resolution and high-light-yield metal halides, in particular the bromides and iodides [3-9]. Due to their narrow band-gaps, they can generate more free electron-hole pairs as products of ionization. In theory, this type of scintillator material would be expected to produce a high scintillation light yield. Because the number of detected photons by the photomultiplier tube (PMT) directly contribute to the energy resolution of inorganic scintillators (the so-called the counting statistics contribution), the metal halides with high light yields tend to achieve excellent energy resolutions of about 3% at 662 keV [10]. Besides the fundamental limit dictated by counting statistics, the energy resolution is also partially determined by the non-proportionality (nPR) contribution of inorganic scintillators. The nPR is the nonlinear dependence of the total light yield on the amount of ionization energy deposited in the scintillator [10]. The metal halides composed of heavy anions, such as bromine and iodine, feature a low optical phonon frequency that allows a slow thermalization of charge carriers [11,12]. When the heavy halides have small hot-electron group velocity, a small radial distribution of hot electrons is expected. As a consequence, the hot electrons do not encounter serious trapping that causes nonlinear quenching before they radiatively recombine with the self-trapped holes in the track core [11,12]. A low probability of non-radiative quenching can secure a proportional light yield response, and positively contribute to the improvement of energy resolution.

In contrast, the oxide scintillators have the advantages of desirable density, high atomic number, and excellent physical and chemical stability need for many practical applications, but they commonly have lower light yield and worse energy resolution than that of heavy metal halides. In principle, oxides with larger band-gaps will produce fewer free charge carriers, and the fast thermalization of charge carriers in most oxides tends to

decrease the charge separation and thus causes the nonlinear quenching, which leads to a nonproportional light yield response and results in worse energy resolution than heavy metal halides [11,12]. However, the general understanding of nPR response is still incomplete so far because it has been shown to depend on temperature, host composition, dopant concentration, and crystal structure, but not in a coherent or predictable way [13,14]. Comparatively speaking, improvement of the energy resolution of oxide scintillators through enhancing light yield is a more feasible approach because: i) the light yields of most oxides are still far below their theoretical values and the fundamental limit of counting statistics of about 60,000 photons/MeV [10]; ii) cation-alloying and ion-codoping approaches have been able to effectively reduce the deleterious trapping of the migrated charge carriers caused by certain types of point defects, resulting in slow scintillation component and/or afterglow and light yield loss [15,16]. The improvement of scintillation yield and energy resolution of oxides and halides via cation-alloying and ion-codoping are shown in FIG. 1. The scintillation properties of classical $Bi_4Ge_3O_{12}$ (BGO) [17] and $YAlO_3$:Ce (YAP:Ce) [18] scintillators are also plotted in FIG. 1 for comparison.

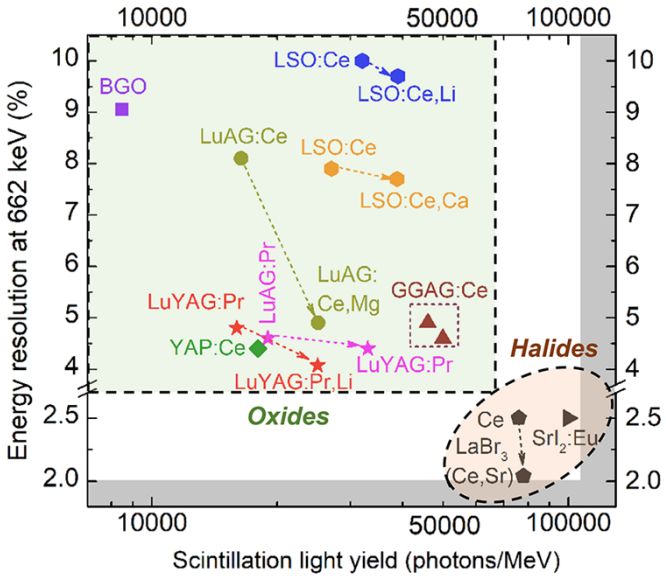

FIG. 1 Advances in cation-alloying and ion-codoping of oxide and metal halide scintillators toward high light yield and gamma-ray spectral resolution. Scintillation properties of BGO and YAP:Ce, are also plotted for comparison. The grey regions are not achievable so far. The data are taken from Refs. [16-24].

The multicomponent aluminate garnets $Gd_3Ga_3Al_2O_{12}$:Ce (GGAG:Ce) and $(Lu_{0.75}Y_{0.25})_3Al_5O_{12}$:Pr (LuYAG:Pr) are successful examples of cation-alloyed oxide scintillators. The partial replacement of Al^{3+} in $Lu_3Al_5O_{12}$:Ce (LuAG:Ce) with Ga^{3+} lowers the band-gap, eliminating the shallow traps induced by antisite defects, while the complete replacement of Lu^{3+} with Gd^{3+} reduces thermal quenching by increasing the energy gap

between the Ce^{3+} $5d_1$ state and conduction band minimum (CBM) [15]. Because the ^{176}Lu is naturally radioactive, the replacement of Lu^{3+} with Gd^{3+} could reduce the continuum background and broaden its applications, such as low-background detection. The resulting GGAG:Ce can achieve a light yield of 56,000 photons/MeV [25], the highest value reported for oxide scintillators, and an energy resolution of 4.9-5.1% at 662 keV measured with an avalanche photodiode [23,25]. Similarly, Y alloying can effectively increase the light yield of LuAG:Pr to 33,000 photons/MeV by burying the shallow electron traps in the conduction band, and achieve an excellent energy resolution of 4.4% at 662 keV measured with a photomultiplier tube [24].

Co-doping is also beneficial to the enhancement of scintillation yield and energy resolution of oxide scintillators through defect engineering. For example, Ca^{2+}-co-doping can substantially enhance the light yield of Lu_2SiO_5:Ce (LSO:Ce) from about 30,000 to 38,000 photons/MeV [16]. This improvement was attributed to the dissociation of spatially-correlated oxygen vacancies (V_O) and cerium centers by the formation of $\{Ca_{Lu}+V_O\}$ complexes, allowing a more efficient migration of charge carriers to activators [26]. Because the nPR response of LSO:Ce is independent of Ca^{2+} co-dopant concentration, the improvement of energy resolution from ~10% to 7.3% at 662 keV by Ca^{2+} co-doping was ascribed to the enhanced light yield [27]. Upon Mg^{2+} co-doping, the energy resolution of LuAG:Ce ceramics was greatly improved from 9.6% to 4.9% at 662 keV due to an 66% increase of light yield by defect reduction [22].

Recently, lithium (Li) co-doping was found to favor the enhancement of scintillation yield of high temperature complex oxides, such as oxyorthosilicates [28,29] and aluminate garnets [21,30-31]. In LSO:Ce single crystals, the site occupation of Li ions plays a critical role in determining the scintillation yield. By occupying different sites, Li dopants can either suppress or promote the formation of oxygen vacancies [29]. With an appropriate amount of Li co-doping, such as 0.5 at%, the light yield of LSO:Ce can be improved from 30,000 to 39,000 photons/MeV [28]. Another exciting discovery is that, due to a 30% increase of light yield by Li^+ co-doping, the energy resolution at 662 keV of the LuYAG:Pr garnet scintillator was improved from 4.8% to 4.1%, the best result ever reported for single-crystalline oxides [21]. At this time, there are some hypotheses about the roles played by Li in aluminate garnets. Li ions were proposed to occupy only the interstitial spaces in $Y_3Al_5O_{12}$:Ce (YAG:Ce) and Lu substitutional sites in $Lu_3Al_5O_{12}$:Ce (LuAG:Ce) [32]. The proposed site occupancy of Li ions seems to explain well the non-conversion of Ce oxidation state in Li-codoped YAG:Ce [30] and partial conversion of stable Ce^{3+} to Ce^{4+} in Li-codoped LuAG:Ce due to the charge compensation effect [31]. However, a small variation of the Ce^{4+}-related charge transfer band in the LuAG host induced by Li co-doping suggests that Li ions only convert a very small amount of stable Ce^{3+} to Ce^{4+} in LuAG:Ce [31], in contrast to the

cases of divalent ions (Ca^{2+} and Mg^{2+}) co-doped LuAG [33,34]. Moreover, the effect of Li^{+} co-doping on defect structures in LuAG is also different from that of divalent co-doping, as confirmed by thermoluminescence measurements [22,31]. Thus, it is important to comprehensively investigate the roles of Li co-dopants for determining the defect structure and improving the scintillator performance.

In this work, we aim to clarify the role of Li regarding the significant improvement of LuYAG:Pr scintillation performance. Such understanding should enable the future composition design of high-light-yield and high-energy-resolution oxide compositions for gamma-ray spectroscopy applications. This work is organized as follows. First, we report the scintillation properties of 10 mm^3 LuYAG:Pr and LuYAG:Pr,0.8 at% Li single crystals, including the scintillation yield, the gamma-ray energy resolution, and the scintillation decay time. Second, the effects of Li codoping on the Pr valence state and the luminescence properties are shown by optical absorption spectra, photoluminescence emission and excitation, and photoluminescence decay kinetics. Third, the preferential Li site occupation is revealed by ^{7}Li nuclear magnetic resonance (NMR) measurement and density-functional theory (DFT) calculations. Then, the atomic-level defect structures in non-codoped and Li-codoped LuYAG:Pr crystals are studied by thermoluminescence measurement and DFT calculations. Finally, the positron annihilation lifetime spectroscopy (PALS) measurement is used to clarify the effects of Li co-doping on cation-vacancy type defects.

II. EXPERIMENTAL AND THEORETICAL METHODS

A. Crystal growth

The 32 mm diameter $(Lu_{0.75}Y_{0.25})_3Al_5O_{12}$:0.2 at% Pr and $(Lu_{0.75}Y_{0.25})_3Al_5O_{12}$:0.2 at% Pr, 0.4 at% Li crystals were grown by the Czochralski method. The as-grown boules are transparent, colorless, and inclusion-free. The growth details can be found in Ref. 21. The boules were cut into 5 mm^3 and 10 mm^3 sizes for measurements.

B. Optical property measurements

Optical absorption spectra were measured with a Varian Cary 5000 UV-VIS-NIR spectrophotometer in the 200-800 nm range.

Photoluminescence (PL) emission and excitation spectra were measured with a HORIBA Jobin Yvon Fluorolog-3 spectrofluorometer. The excitation light passed through an excitation monochromator with a 1 nm bandpass to ensure monochromaticity. Similarly, the emission monochromator was set at a

1 nm bandpass to select emission light of a specific wavelength. A 450W continuous xenon lamp was used as the excitation source in emission and excitation spectra.

Photoluminescence decay was measured on the same spectrofluorometer using a time-correlated-single-photon counting module. HORIBA Jobin Yvon NanoLEDs (pulsed light-emitting diodes) were used as the excitation source. The duration of the light pulse was shorter than 2 ns and therefore was not deconvoluted from the much longer decay profiles.

C. Scintillation property measurements

The absolute light yield measurement was recorded by using a pulse processing chain consisting of a Hamamatsu R2059 photomultiplier tube (PMT) operated at -1500 V_{bias}, an Ortec 672 Amp, a Canberra model 2005 pre-Amp and a Tukan 8k multi-channel analyser. Each sample was directly coupled to the PMT using mineral oil, and a PTFE-lined dome-shaped reflector with a 50 mm diameter was used to maximize the collection of light. The photoelectron yield of the samples was calculated by using the single photoelectron peak method. Measurements on the samples were made at a gain of 5 with 10 μs shaping time to provide full light integration. The reproducibility of light yield is ±5%. The energy resolution was measured using a 5 cm diameter high quantum efficiency Hamamatsu R6231-100 PMT. This PMT was operated at -1.0 kV V_{bias}.

For the afterglow measurements, the crystals were coupled to a Hamamatsu R2059 PMT covered with Tetratex TX3104 PTFE membrane. The crystals were irradiated with x-rays at room temperature for 15 min, after which X-ray beam was cut off within 1 s and the luminescence emitted from crystal was recorded as a function of time.

Scintillation decay times were measured using a time-correlated single-photon counting setup under ^{137}Cs source excitation.

D. Nuclear Magnetic Resonant measurements

The solid-state ^{7}Li NMR spectrum of a Li-codoped LuYAG:Pr sample was acquired with a Bruker Avance III 400 MHz magnet operating at 155.5 MHz using a 3.2 mm MAS broad band probe (zirconia rotors). The sample was spun at magic angle spinning of 15 kHz at 20°C. The ^{7}Li chemical shift was referenced to 1M LiCl at 0 ppm. A single pulse sequence was employed to record this data with a recycle delay (d1) of 10 s. About 90000 scans were accumulated for reasonable signal-to-noise.

E. Positron Annihilation Lifetime Spectroscopy measurements

The Positron Annihilation Lifetime Spectroscopy (PALS) measurements were performed using a ~10 μCi ^{22}Na source sealed between two ~8 μm thick Kapton films. In the experiment, the source was sandwiched between two identical cubic crystals such that the whole solid angle of the source is covered by the sample. Two cylindrical plastic scintillators measuring 1 inch in diameter by 1 inch long were used in combination with two Hamamatsu H3378-50 PMT to detect the 1274 keV start signals from the source in coincidence with the 511 keV annihilation gamma photons as the stop signals. Two Ortec 583 constant fraction discriminators were used to set the thresholds for the start and stop pulses. The PALS histograms were fitted using POSFIT, and the typical time resolution of the system is ~210 ps. In each spectrum, a total number of more than 1.6×10^6 coincident events were recorded.

F. Thermoluminescence measurements

For each thermoluminescence (TL) measurement, a sample was mounted on the cold finger of the cryostat. The pressure was reduced to 20 mTorr and the sample was then heated to 550 K to ensure that all traps were empty in the temperature range of interest. The samples were cooled to 10 K and irradiated by an X-ray generator (X-ray Model; CMX003) at 35 kV and 0.1 mA for 15 min. Subsequently, the sample was heated to 550 K at a rate of 3 K/min; noise from thermionic emissions precluded the acquisition of good quality data above this temperature. A Hamamatsu H3177 PMT optically coupled to the cryostat's light transport interface was used to measure the spectrally unresolved emission from the sample. The PMT current signal was transformed into a voltage signal using standard NIM electronics. A National Instruments 6002-E data acquisition card was then used to digitize this voltage signal. Software developed in-house was used to correlate the sample temperature with the signal intensity. The measured TL glove curves were corrected by using the temperature dependence of Pr^{3+} emission efficiency for both non-Li codoped and Li-codoped LuYAG:Pr samples.

G. Density Functional Theory calculations.

All calculations are based on density functional theory (DFT) [35,36] implemented in the VASP code [37]. The interaction between ions and electrons is described by the projector augmented wave method [38]. The total energy is calculated using the Perdew-Burke-Eznerhof (PBE) exchange correlation functional [39], a 2×2×2 k-point mesh, and a kinetic energy cutoff of 500 eV. The atomic positions are relaxed until the forces are less than

0.02 eV/Å. The theoretically optimized lattice constant of $Lu_3Al_5O_{12}$ (a = b = c =11.959 Å) is in excellent agreement with the experimental value of 11.906 Å [40].

The formation energy of a defect is given by:

$$\Delta H = (\mathrm{E}_D - \mathrm{E}_h) - \sum_i n_i(\mu_i + \mu_i^{ref}) + q(\varepsilon_{VBM} + \varepsilon_f), \quad (1)$$

where E_D and E_h are the total energies of the defect-containing and the host (i.e. defect-free) supercells. The formation of a defect in a material involves an exchange of atoms with their respective chemical reservoirs. The second term in Eq.(1) represents the change in energy due to such exchange of atoms, where n_i is the difference in the number of atoms for the *i*'th atomic species between the defect-containing and defect-free supercells. μ_i is the relative chemical potential for the *i*'th atomic species, referenced to the chemical potential of its elemental phase μ_i^{ref}. Here, the chemical potentials of the elemental phases of Lu, Al, Li, and O are taken as the chemical potentials of Lu, Al, and Li metals and half of the energy of an O_2 molecule, respectively. The third term in Eq. (1) represents the change in energy due to the exchange of electrons with its reservoir. ε_{VBM} is the energy of the valence band maximum (VBM) and ε_f is the Fermi energy relative to the VBM. Corrections to the defect formation energy due to potential alignment (between the host and a charged defect supercell) and image charge corrections [41] were applied wherever appropriate.

The chemical potentials in Eq. (1) are subject to a series of thermodynamic constraints under the equilibrium growth condition. To maintain the stability of $Lu_3Al_5O_{12}$ during growth, the chemical potentials of Lu, Al, and O should satisfy,

$$3\mu_{Lu} + 5\mu_{Al} + 12\mu_{Al} = \Delta H_f(Lu_3Al_5O_{12}), \quad (2)$$

where $\Delta H_f(Lu_3Al_5O_{12})$ is the enthalpy of formation for $Lu_3Al_5O_{12}$.

To avoid the formation of the binary oxides (Lu_2O_3, Al_2O_3, and Li_2O) and elemental phases of Lu, Al, O, and Li, the following constraints on chemical potentials are applied:

$$2\mu_{Lu} + 3\mu_O \le \Delta H_f(Lu_2O_3),$$
$$2\mu_{Al} + 3\mu_O \le \Delta H_f(Al_2O_3),$$
$$2\mu_{Li} + \mu_O \le \Delta H_f(Li_2O),$$
$$\mu_{Lu} < 0, \mu_{Al} < 0, \mu_O < 0, \mu_{Li} < 0. \quad (3)$$

Here, $\Delta H_f(Lu_2O_3)$, $\Delta H_f(Al_2O_3)$ and $\Delta H_f(Li_2O)$ are the enthalpies of formation for Lu_2O_3, Al_2O_3, and Li_2O, respectively.

The defect concentration can be calculated by

$$N = N_{site} e^{\frac{-\Delta H}{k_B T}}, \quad (4)$$

where N_{site} is the number of available atomic sites for doping, ΔH is the defect formation energy calculated by Eq. (1), k_B is the Boltzmann constant, and T is temperature.

III. RESULTS AND DISCUSSION

A. Improved scintillation yield and energy resolution in Li-codoped LuYAG:Pr single crystals

We have reported the beneficial effects of Li co-doping on the light yield and the energy resolution of LuYAG:Pr single crystals [21]. With Li co-doping, the light yield and energy resolution of 5 mm^3 LuYAG:Pr single crystals can be improved from 16,000 to 25,000 photons/MeV, and from 4.8 to 4.1% at 662 keV, respectively. Here, we further explore the scintillation characteristics of larger-sized (10×10×10 mm^3) Li-codoped LuYAG:Pr crystals, which is comparedwith that of non-codoped LuYAG:Pr. The energy resolution of non-codoped and Li-codoped LuYAG:Pr at 662 keV was evaluated with a Hamamatsu R6231-100 super bialkali PMT under ^{137}Cs irradiation. The pulse height spectra are plotted in FIG. 2(a). The energy resolution of a 10×10×10 mm^3 non-codoped LuYAG:Pr crystal can be improved from 5.3 to 4.3% at 662 keV upon 0.4 at% Li codoping. The absolute light yield of 10 mm^3 non-codoped and Li-codoped LuYAG:Pr samples was evaluated with a calibrated Hamamatsu R2059 PMT under ^{137}Cs irradiation (see FIG. 2(b)). The spectrum of a BGO reference is plotted for comparison. The emission-weighted quantum efficiency (EWQE) of PMT used is considered for each sample. Light yields of 15,600 and 24,800 photons/MeV were estimated for 10×10×10 mm^3 non-codoped and Li-codoped LuYAG:Pr crystals, respectively. Scintillation decay profiles at room temperature are shown in FIG. 2(c) for non-codoped and Li-codoped LuYAG:Pr samples. All decay profiles are approximated by three exponentials, corresponding to the prompt and delayed radiative recombinations at the Pr^{3+} centers. The decay components of LuYAG:Pr are 45 ns (98.7%), 336 ns (0.8%), and 1420 ns (0.5%). The decay components of Li-codoped LuYAG:Pr are 56 ns (95.9%), 400 (2.4%), and 1520 ns (1.7%). The physical and scintillation properties of 10×10×10 mm^3 non-codoped and Li-codoped LuYAG:Pr are listed in Table I to compare with other Li-dodoped aluminate garnet scintillator samples with comparable size.

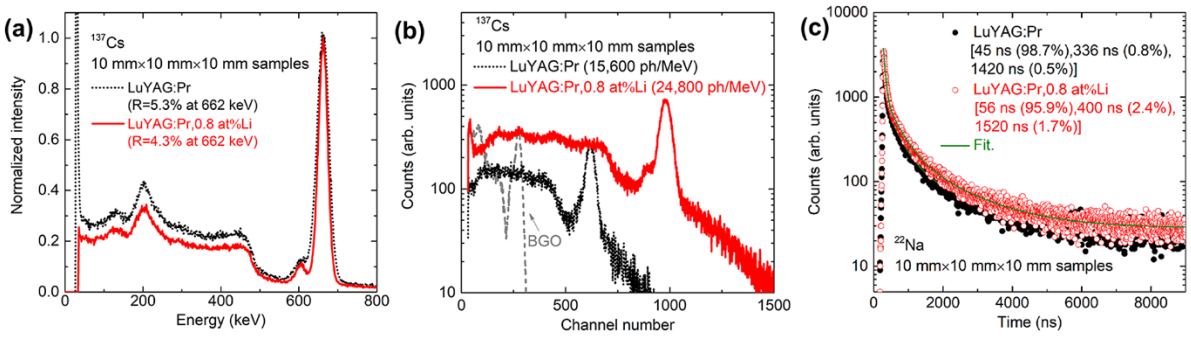

FIG. 2 (a) Gamma-ray energy resolution evaluation of 10×10×10 mm^3 LuYAG:Pr and LuYAG:Pr,Li single crystals acquired by a high quantum efficiency Hamamatsu R6231-100 PMT. (b) Absolute light yield evaluation of 10 mm^3 LuYAG:Pr and LuYAG:Pr,Li single crystals by using a calibrated Hamamatsu R2059 PMT. The pulse height spectrum of a BGO standard sample with a light yield of 8,800 photons/MeV is plotted for comparison. (c) Scintillation decay profiles of 10 mm^3 LuYAG:Pr and LuYAG:Pr,Li single crystals recorded under ^{22}Na gamma-ray irradiation.

TABLE I. Physical and scintillation properties of non-codoped and Li-codoped aluminate garnets.

Samples	Density (g/cm^3)	Z_{eff}	Dimension (mm)	E.R. [a] (%)	L.Y.[b] (photons/MeV)	τ [c] (ns)/I (%)	Ref.
YAG:Ce	4.56	35.0	∅10×10	6.8	100% [d]	111/42; 241/32; 1380/26	[30]
YAG:Ce,Li				9.7	~140% [d]	127/94; 762/6	
LuAG:Ce	6.67	58.9	∅15× 1.5	NA	14,760	69/41; 1120/59	[31]
LuAG:Ce,Li				NA	17,740	61/43; 1240/57	
LuYAG:Pr	6.20	55.0	10×10×10	5.3	15,600	45/98.7;336/0.8;1420/0.5	This work
LuYAG:Pr,Li				4.3	24,800	56/95.9; 400/2.4; 1520/1.7	

a) "E.R." is signified for gamma-ray energy resolution at 662 keV.
b) "L.Y." is signified for scintillation light yield.
c) "τ"is signified for scintillation decay constant.
d) The absolute light yields were not reported in Ref. 31. The relative light yield of YAG:Ce, 5 at% Li was compared to that of non-codoped YAG:Ce, which is regarded as "100%".

B. Oxidation state of praseodymium ions and luminescence properties of Pr^{3+} centers

Aliovalent co-doping, such as Mg^{2+} co-doping, can promote the conversion of stable Pr^{3+} to Pr^{4+} in LuAG:Pr single crystals. It leads to a reduction in the overall scintillation efficiency due to an enhanced overlapping between Pr^{3+} 5d-4f emission band and the Pr^{4+}-O^{2-} charger transfer absorption band [42]. To study the effect of Li codoping on the Pr oxidation state in the LuYAG host, the optical absorption spectra of non-codoped and Li-codoped LuYAG:Pr crystal samples were recorded and plotted in FIG. 3(a). For both samples, we can only observe the prominent absorption peaks located at 285 and 240 nm related to the Pr^{3+} 4f-5$d_{1,2}$ transitions, along with several weak peaks between 450 and 650 nm due to the Pr^{3+} 4f-4f transitions, such as $^3H_4 \rightarrow {}^3P_{2,1,0}$ and $^3H_4 \rightarrow {}^1D_2$. The charger transfer transition associated with the stable Pr^{4+} ions, a broad band with an onset situated around 600 nm

[42], cannot be identified in either samples. By using X-ray absorption spectroscopy (XAS), we have confirmed that the oxidization sate of Pr in the LuAG crystal (analogous to LuYAG) grown under the same condition is 100% 3+ [43]. Therefore, it is reasonable to believe that praseodymium ions maintain purely 3+ with Li codoping in the LuYAG host. Very similarly, codoping Li into YAG:Ce crystals does not convert the oxidation state of cerium ions from 3+ to 4+, as confirmed by XAS measurements [30].

The effect of Li co-doping on optical properties of stable Pr^{3+} centers was clarified by investigating the spectral properties and decay kinetics. The normalized room temperature PLE and PL spectra of non-codoped and Li-codoped LuYAG:Pr are shown in FIG. 3(b). For both compositions, the excitation spectrum monitored at an emission wavelength of 322 nm corresponding to Pr^{3+} $5d_1$-4f de-excitation consists of two dominant bands associated with the transitions from 4f ground state to the $5d_{1,2}$ excited states of Pr^{3+}. The emission spectrum excited under 277 nm includes two dominant band emissions at 322 nm and 380 nm related to the radiative transitions from Pr^{3+} $5d_1$ to ^3H_x (x=4, 5, 6) and $^3F_{3(4)}$ 4f states, and several relatively weak line emissions between 450 and 550 nm related to the Pr^{3+} 4f-4f radiative transitions. They are in good agreement with previous results of LuYAG:Pr ceramic counterparts [44]. The PL decay kinetics of non-codoped and Li-codoped LuYAG:Pr were studied under direct excitation of the 4f-$5d_1$ transition. Both PL decay profiles shown in FIG. 3(c) can be well fitted by a single exponential function. The decay constant is 21 ns for non-codoped LuYAG:Pr and 20 ns for Li-codoped LuYAG:Pr, respectively, similar with the published result of 21 ns for LuAG:Pr crystals [42]. The spectral and decay properties indicate a negligible effect of Li codoping on luminescence properties of stable Pr^{3+} centers in LuYAG host.

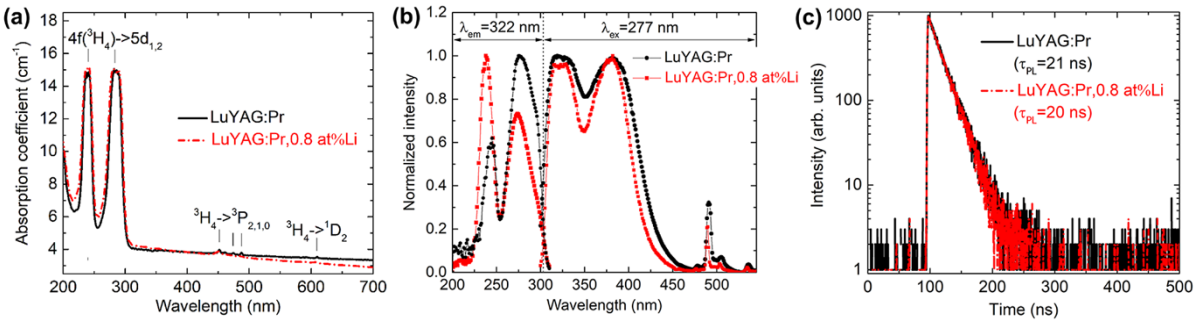

FIG. 3 Optical properties of non-codoped and Li-codoped LuYAG:Pr single crystals: (a) optical absorption spectra; (b) photoluminescence excitation (λ_{em}=322 nm) and emission (λ_{ex}=277 nm) spectra; (c) photoluminescence decay profiles monitored at λ_{ex}=295 nm and λ_{em}=322 nm.

C. Preferential site occupancy of Li ions studied by ^{7}Li solid-state NMR and DFT calculations

Because of the unchanged valence state of Pr ions after Li codoping, the valence state mismatch between monovalent Li codopant and the trivalent host cations (Lu, Y, and Al) will inevitably lead to defect structure alternation due to charge compensation. Since the defect structure variation induced by codopants is directly determined by the site occupancy of codopants, the understanding of preferential site occupancy of Li ions is critical to clarify the defect structure alteration. In many oxides, Li ions tend to occupy multiple sites in the host lattice, such as interstitial site and substitutional sites [45-47]. This diversity in the site occupation of Li ions can play a vital role in modifying the defect structure [45-47]. Here we use the ^{7}Li solid-state NMR technique and the DFT calculation to reveal the preferential site occupancy of Li in the LuYAG host.

The ^{7}Li-MAS-NMR spectrum of LuYAG:Pr,0.8 at% Li shown in FIG. 4 can be well de-convolved into three ^{7}Li resonance signals. The downfield signal located at 1.61 ppm contributes 48% of the total ^{7}Li signal, and the signal at 0.07 ppm contribute 51% of the total ^{7}Li signal, while 1% of ^{7}Li exhibit an upfield signal at -2.80 ppm. There are three different occupation sites of Li ions but two of them dominate. We conduct DFT calculation to estimate the formation energies of different Li occupation sites by considering the practical growth temperature and atmosphere. To simplify the calculation, the LuAG host that has the same crystal structure with the 25% Y alloyed LuAG was chosen to conduct the calculations of formation energies of Li dopants. We considered substitutional Li on Lu and Al sites (which are double acceptors) and Li interstitials (which are single donors). There are two inequivalent Al sites (the 24d site with the Td symmetry and the 16a site with the Oh symmetry). DFT calculations show that Li_{Al}^{2-} is more stable on the 24d site than on the 16a site by 0.32 eV. Thus, Li_{Al}^{2-} in the rest of the paper refers to the 4-fold coordinated Li_{Al}^{2-} on the 24d site as shown in FIG. 5(b). The relative stability between Li_{Al}^{2-} and Li_{Lu}^{2-} depends on chemical potentials. Under the O-poor condition, which is the typical growth condition, Li_{Al}^{2-} is more stable than Li_{Lu}^{2-} by 0.23 eV. Regarding Li interstitials, Li_i, there are two possible sites with four and six oxygen neighbors as shown in FIGs. 5(a) and (c), respectively. The 6-fold coordinated Li_i is found to be slightly more stable than the 4-fold coordinated Li_i (by only 7 meV). With heavy Li doping, the Fermi level should be pinned by the lowest-energy Li-induced donor (Li_i) and acceptor (Li_{Al}^{2-}) defects (more details in Sec. III-D). Thus, the three most probable Li doping sites in LuYAG are 4-fold coordinated Li_{Al} and 4-fold and 6-fold coordinated Li_i .

The chemical shift of the ^{7}Li NMR signal is sensitive to the local environment of the atoms, such as coordination numbers and the mean bond length [48,49]. In crystalline oxides, the ^{6}Li (or ^{7}Li) shows an upfield shift as the coordination number of Li increases with the concentration of oxygen [48]. Thus, we ascribe the

upfield signal at -2.8 ppm to the 6-fold coordinated Li_i site. The 4-fold coordinated Li_{Al} and Li_i have different mean $<r_{Li-O}>$ bond lengths. For the asymmetrical Li_i site, four different kinds of oxygen sites present around the lithium with r_{Li-O}=1.777, 1.776, 1.825, and 1.923 Å. The Li_{Al} site coordinates with four oxygens with the same bond length of 1.924 Å. Under the same coordination number, the longer mean bond length tends to provide less shielding from the full external magnetic field, and leads to a more positive chemical shift of this nucleus. Thus, the ^{7}Li signal at 1.61 ppm and 0.07 ppm can be assigned to 4-fold coordinated Li_i and 4-fold coordinated Li_{Al}, respectively, both of which are the dominant Li occupancy sites.

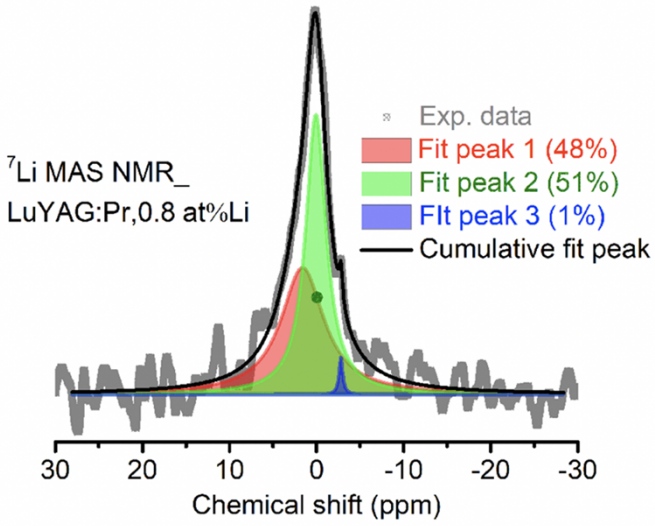

FIG. 4 (a) ^{7}Li NMR spectrum of LuYAG:Pr,0.8 at% Li. The black line is the superposition of three fitted Lorentzian peaks. The ratio of the three ^{7}Li peaks at 1.61 ppm (red peak), 0.07 ppm (green peak), and -2.80 ppm (blue peak) is 48%, 51%, and 1%, respectively.

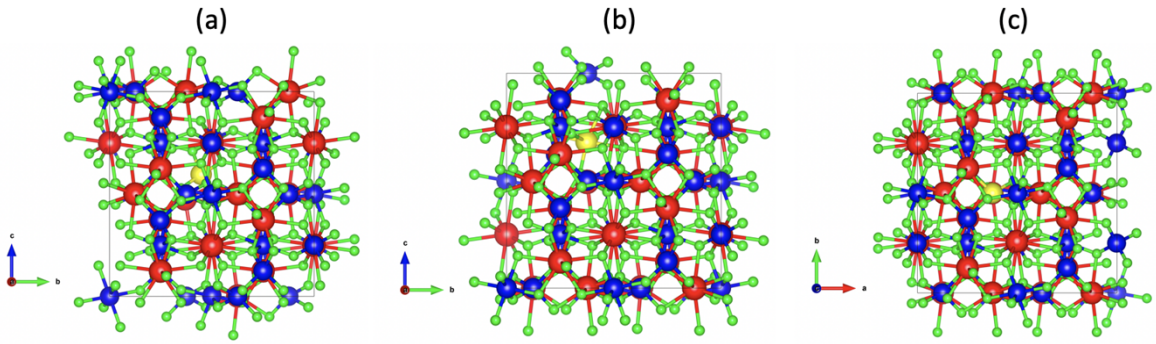

FIG. 5 Structure configurations containing 4-fold coordinated Li_i interstitial defect (a), 4-fold coordinated Li_{Al} substitute defect (b), and 6-fold coordinated Li_i interstitial defects (c). Green, red, blue, and yellow spheres represent O, Lu, Al, and Li atoms, respectively.

D. Defect structures studied by TL measurements and DFT calculations

Thermoluminescence study of defect structure

The thermoluminescence technique and DFT calculations were used to understand the Li codoping-related defect structure variation in LuYAG:Pr after Li codoping from experimental and theoretical insights. The TL glow curves of non-codoped and Li-codoped LuYAG:Pr crystals after X-ray irradiation at 10 K are shown in FIG. 6(a). There are three distinct differences in the Li-codoped sample: i) appearance of new TL peaks below 150 K; ii) a significant suppression of TL peaks between 200 and 300 K; and iii) appearance of new TL peaks between 300 and 450 K. Before the discussion of the assignment of TL peaks, we first analyze the trap depth of all peaks. To quantitatively determine the trap depth, the modified general-order kinetics expression describing TL intensity I as a function of temperature T is used to fit the glow curve [50]:

$$I(T) = sn_0 \exp\left(-\frac{E_t}{\kappa_B T}\right) \times \left\{\frac{(l-1)s}{\beta} \times T \times \exp\left(-\frac{E_t}{\kappa_B T}\right) \times \left[\left(\frac{\kappa_B T}{E_t}\right) - 2\left(\frac{\kappa_B T}{E_t}\right)^2 + 6\left(\frac{\kappa_B T}{E_t}\right)^3\right] + 1\right\}^{l/(1-l)} \quad (5)$$

where n_0 is the concentration of trapped charges at t=0, E_t the energy level of the trap, κ_B the Boltzmann constant, l the kinetic order, s the frequency factor, and β the heating rate (3 K/min in this measurement). Due to the similarity between the TL curves of LuYAG:Pr crystal and the ceramic counterpart [44], we used the TL parameters derived from the "partial cleaning and initial rise method" published in Ref. 44, such as trap depth and frequency, as initial fitting parameters. The fitting curves agree well with the experimental data (see FIG. 6(b) and (c)). The TL peak temperature, trap depth, and frequency are presented in Table II. The detrapping time τ of the trap at temperature T can be calculated from the equation below [51]:

$$\tau = s^{-1} e^{E/kT} \quad (6)$$

The detrapping time of each trap at room temperature is also presented in Table II.

The TL structure between 150 and 200 K related to traps with a depth of 0.41 eV and a lifetime of 10^{-3} s in non-codeped LuYAG:Pr sample should be associated with electron localization at antisite defects (such as Lu_{Al} and Y_{Al}) [50]. In Ce-doped LuAG crystals, the traps related to Lu_{Al} antisite defects are located 0.3-0.5 eV below the conduction band minimum (CBM) [50]. The trap depth of Y_{Al} antiste defects in YAG is about 0.11 eV closer to the CBM than that in LuAG [52]. Because the CBM in a LuAG host shifts downward by 0.07 eV with a 25 at% Y alloying [44], both Lu_{Al} and Y_{Al} antisite defects should be located within the forbidden gap of LuYAG host, not buried in the conduction band.

A series of new TL peaks below 150 K in Li-codoped LuYAG:Pr are attributed to formation of Li-related shallow donors, such as Li_i donor defects that dominate 48% of the Li occupation sites in LuAG. Li codoping can significantly suppress TL peaks between 200 and 300 K corresponding to traps with a depth between 0.48-0.62 eV. The origin of these peaks are unclear, but they cannot be ascribed to native defects V_O [53,54] because the associated TL peaks in LuAG:Pr located above 650 K [55]. The appearance of new TL peaks above 300 K suggests Li codopants introduce deep traps about 0.8-1.0 eV below the CBM. The lifetime of these deep traps are ranging from 10^4 to 10^6 seconds at room temperature, and thus, such traps will cause afterglow. The room temperature X-ray induced afterglow profiles of non-codoped and Li-codoped LuYAG:Pr samples are presented in the inset of FIG. 6(a). The afterglow signal of the Li-codoped LuYAG:Pr sample drops by about two orders of magnitude within the first few seconds after the x-ray cut-off, and decreases gradually afterward. Its afterglow level is one order of magnitude higher than that of non-codoped LuYAG:Pr throughout the entire measurement period. The afterglow enhancement at room temperature suggests the induced deep traps result in a scintillation yield loss.

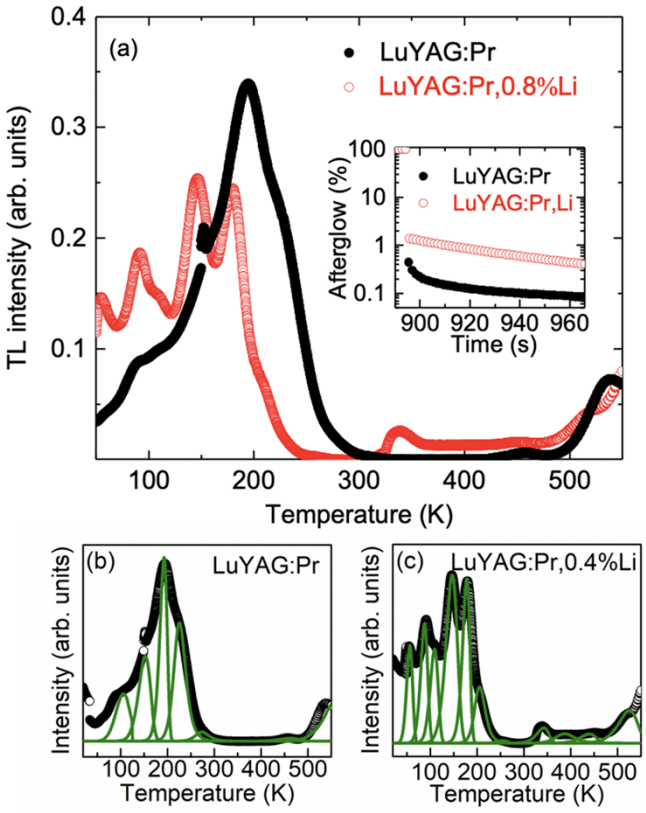

FIG. 6 (a) Corrected TL glow curves of non-codoped and 0.8 at% Li codoped LuYAG:Pr single crystals. Experimental TL glow curves (in black) and fitting curves (in green): (b) non-codoped LuYAG:Pr, (c) LuYAG:Pr,0.8 at% Li.

TABLE II. TL fitting parameters of LuYAG:Pr and LuYAG:Pr,0.8 at%Li. The errors for trap-depth values are about 10%.

Samples	TL peak temperature (K)	Trap depth (eV)	Frequency factor (s^{-1})	Detrapping time at RT (s)
LuYAG:Pr	107	0.06	$\sim 10^{1}$	$\sim 10^{0}$
	149	0.15	$\sim 10^{3}$	$\sim 10^{-1}$
	193	0.41	$\sim 10^{9}$	$\sim 10^{-3}$
	225	0.48	$\sim 10^{9}$	$\sim 10^{-1}$
	280	0.62	$\sim 10^{10}$	$\sim 10^{0}$
	463	0.93	$\sim 10^{8}$	$\sim 10^{7}$
	541	1.09	$\sim 10^{9}$	$\sim 10^{9}$
LuYAG:Pr,Li	53	0.04	$\sim 10^{2}$	$\sim 10^{-2}$
	92	0.05	$\sim 10^{1}$	$\sim 10^{0}$
	110	0.06	$\sim 10^{1}$	$\sim 10^{0}$
	148	0.14	$\sim 10^{3}$	$\sim 10^{-1}$
	179	0.35	$\sim 10^{8}$	$\sim 10^{-3}$
	202	0.46	$\sim 10^{10}$	$\sim 10^{-3}$
	257	0.55	$\sim 10^{10}$	$\sim 10^{-1}$
	343	0.79	$\sim 10^{10}$	$\sim 10^{4}$
	390	0.90	$\sim 10^{10}$	$\sim 10^{5}$
	456	0.97	$\sim 10^{10}$	$\sim 10^{6}$
	526	1.16	$\sim 10^{10}$	$\sim 10^{9}$

We then employ the DFT calculations to determine the type of intrinsic and external defects. Since the 25% Y-alloying does not alter the crystal structure of LuAG, to simplify the calculation procedure, all the DFT calculations were performed on the LuAG matrix instead of LuYAG.

DFT calculations of Intrinsic and extrinsic defects

FIG.6 shows the calculated phase diagram of $Lu_3Al_5O_{12}$. Formation energies of native defects (vacancies, interstitial, antisites, and their complexes) in $Lu_3Al_5O_{12}$ were calculated using chemical potentials corresponding to the points A, B, and C in the phase diagram (FIG. 7). The results are shown in FIG. 8. Li doping introduces a variety of new defects. The calculated formation energies of Li-induced defects are shown in FIG. 9. The low-energy native and Li-induced defects at the O-poor limit as identified in FIG. 8 and 9 are summarized in FIG. 10.

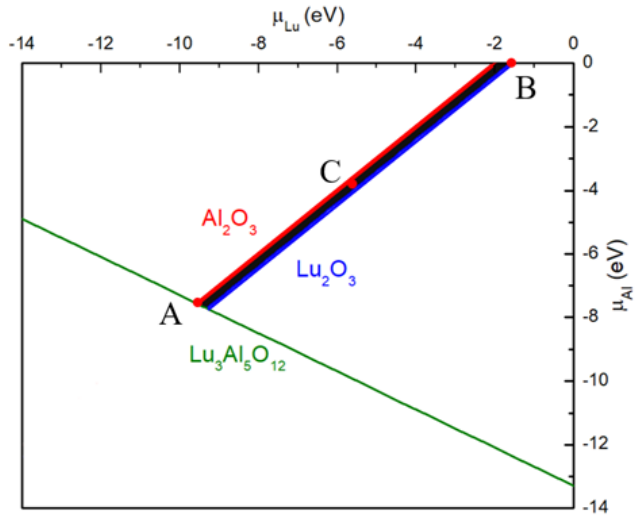

FIG. 7 Phase diagram of $Lu_3Al_5O_{12}$. The narrow black stripe represents the chemical potential region in which $Lu_3Al_5O_{12}$ is stable. Points A, B, and C, which correspond to O-rich and poor limits and an intermediate O chemical potential, are used to calculate defect formation energies.

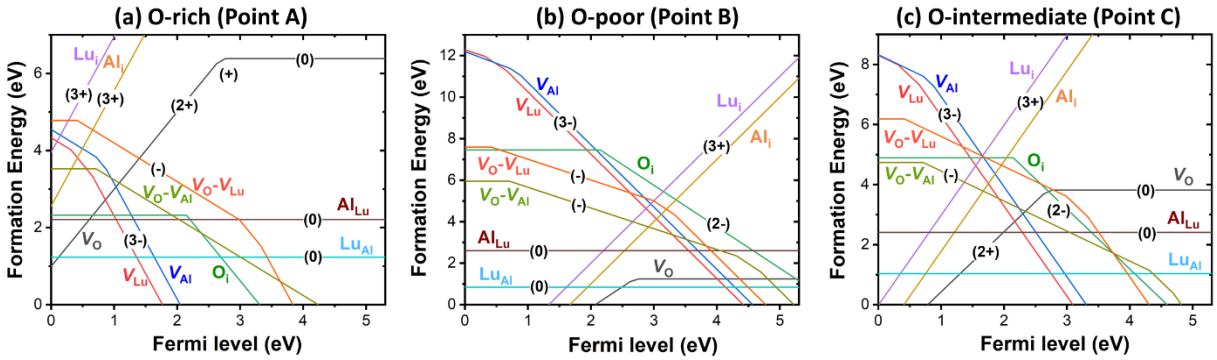

FIG. 8 Formation energies of native defects in $Lu_3Al_5O_{12}$ as a function of the Fermi level at (a) the O-rich limit, (b) the O-poor limit, and (c) an intermediate O chemical potential. The chemical potentials used in (a), (b), and (c) correspond to the points A, B, and C in Figure 6. The slope of a formation energy line represents the charge state of a defect. The point where the slope changes is the charge transition level.

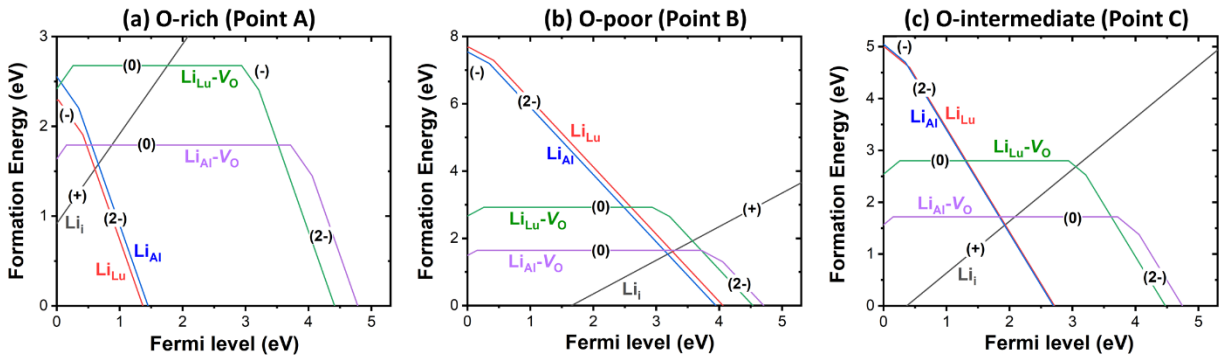

FIG. 9 Formation energies of Li-induced defects in $Lu_3Al_5O_{12}$ as a function of the Fermi level at (a) the O-rich limit, (b) the O-poor limit, and (c) an intermediate O chemical potential. The chemical potentials used in (a), (b), and (c) correspond to the points A, B, and C in Figure 6. The slope of a formation energy line represents the charge state of a defect. The point where the slope changes is the charge transition level.

The antisite defect Lu_{Al} has a low formation energy. At the O-poor limit (the point B in FIG. 6), the calculated concentration of Lu_{Al} is about 1.5% (at the growth temperature of 2036 °C), consistent with the experimental result (about 3.06% Lu_{Al} in LuAG:0.25 at% Ce [56]). The dominant donor defect is the O vacancy (V_O), which is found to be a deep donor. The calculated (2+/+) and (+/0) charge transition levels are 2.67 eV and 2.54 eV below the conduction band minimum (CBM). The dominant acceptor defects are Lu and Al vacancies (V_{Lu} and V_{Al}); the former is more stable than the latter. The calculated hole trapping levels [the (3-/2-) level] of V_{Lu} and V_{Al} are 0.66 eV and 0.89 eV above the valence band maximum (VBM). The Fermi level of the undoped $Lu_3Al_5O_{12}$ is pinned approximately at the crossing point between the formation energy lines of the lowest-energy donor and acceptor defects (blue dashed line in FIG. 10). Li-codoping introduces Li-induced donor and acceptor defects (Li_i^+ and Li_{Al}^{2-}), which can pin the Fermi level deeper inside the band gap (red dashed line in FIG. 10) in the case of heavy Li codoping. Li_i is found to be a shallow donor, which introduces shallow hydrogenic levels. The TL measurement found that the Li codoping indeed introduces some shallow traps with depth less than 0.1 eV (corresponding to the TL peaks below 120K). Li_{Al} and Li_{Lu} introduce hole trapping levels [(2-/-) level], which are calculated to be 0.35 eV and 0.42 eV above the VBM. As can be seen in FIG. 10, the Li codoping introduces new hole traps (Li_{Al}^{2-} and Li_{Lu}^{2-}), but also reduces the concentrations of the deeper hole traps induced by V_{Lu}^{3-} and V_{Al}^{3-}. The TL measurement also indicates Li codoping suppresses some relatively deep traps with depth of 0.48-0.62 eV while introducing some shallower traps of depth of 0.35-0.46 eV. Compared to V_{Lu}^{3-} and V_{Al}^{3-}, Li_{Al}^{2-} and Li_{Lu}^{2-} are

less attractive to holes due to the lower charge state; thus, resulting in lower hole trapping cross sections and shallower hole trapping levels. These defects are likely more effective in hole trapping than Pr activators due to their negative charge states. Therefore, lowering the hole trapping energy and cross sections by Li doping may increase the probability of hole trapping by Pr and improves the light yield.

The lowering of the Fermi level by Li doping increases the concentration of V_O^{2+} and V_O^{+}, which are deep electron traps. Although V_O is an important electron trap in undoped $Lu_3Al_5O_{12}$, it likely has a negligible effect on electron trapping in heavily Pr-doped $Lu_3Al_5O_{12}$. The native defect V_O has a much lower concentration than the Pr dopant and the electron trapping by the deep V_O requires the emission of a large number of phonons, resulting in a much lower trapping probability at V_O than at Pr. Therefore, Li codoping may improve the hole trapping efficiency by Pr while having a negligible effect on the electron trapping by Pr.

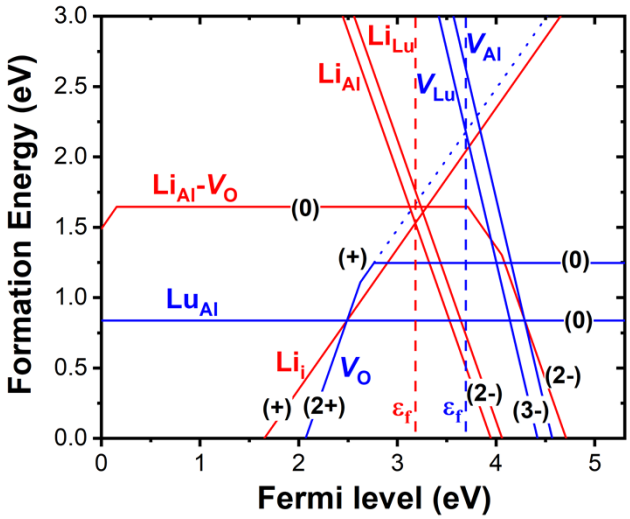

FIG. 10 Formation energies of low-energy native defects (blue lines) and Li-induced defects (red lines) in $Lu_3Al_5O_{12}$ as a function of the Fermi level at the O-poor limit (the point B in Figure 6). The maximum Li chemical potential is used. The slope of a formation energy line represents the charge state of a defect. The point where the slope changes is the charge transition level. The blue dashed line indicates the Fermi level in undoped $Lu_3Al_5O_{12}$ (pinned by V_O^{+} and V_{Lu}^{3-}). The red dashed line indicates the Fermi level in Li-doped $Lu_3Al_5O_{12}$ (pinned by Li_i^{+} and Li_{Al}^{2-}).

E. Verification of reduction of cation vacancy by PALS method

Positron lifetime spectroscopy is a highly informative technique for microscopic characterization of vacancy-type defects. The absence of a positive charge in a cation vacancy provides an attractive potential that

traps positrons at this site, and this trapping leads to significant changes in measured positron lifetime. As the vacancy lacks the electrons of the missing atom, the electron density is lower leading to a longer positron lifetime. Positron spectroscopies are typically sensitive to trapping at vacancy centers with concentrations as low as 0.1 ppm. Since different types of defects have different electron densities and different positron annihilation lifetimes, the PALS experiments yield detailed information on the states and structure of cation-vacancy-related defects. Here we utilize this technique to verify the reduction of cation vacancy by Li codoping proposed above.

PALS spectra were recorded from the LuYAG:Pr and Li-codoped LuYAG:Pr samples (shown in FIG. 11). Three lifetime components gave the best fit for both spectra with good fitting variance. Table III below shows the three-lifetime fitting results of the crystals. It is estimated that the source has contributed approximately 15% to the ~380 ps component. The first two lifetimes (τ_1 and τ_2) are from direct positron annihilation with the electrons of the materials, and the third long lifetime (τ_3) is due to the annihilation of positronium – a metastable bound state of a positron and an electron. Their corresponding intensities (I_1, I_2, and I_3) represent the fractions of positrons annihilating under each lifetime.

In general, the positronium lifetime (τ_3) can be straightforwardly correlated to the size of the free volume voids in materials since it is not sensitive to the specific chemistry of the material. Here, the 3.1 ns lifetime can be converted to a pore size of 0.74 nm in diameter if using the well-established Tao-Eldrup model. The I_3 for both samples are below 2%. This component might be attributed to vacancy clusters of multiple missing atoms or larger voids with relatively low concentration. However, it is quite possible that this component can be partially or fully attributed to geometric effects due to positronium annihilation in the air gap between the sample and the source, especially for the Li co-doped sample of which the I_3 is only ~0.5%. Therefore, the origin of this component is not completely clear, and is not the focus of this study.

Most of the positrons annihilate directly with electrons instead of forming positronium since the total intensity of positron annihilation (sum of I_1 and I_2) is close to 100% for non-codoped and Li-codoped samples. In general, the two positron lifetimes, τ_1 and τ_2, may correspond to positrons annihilating in delocalized state and in trapping vacancies respectively. The first component may also be related to defects of high concentration such that almost all of the positrons are trapped. For example, τ_1 is related to single vacancies, while τ_2 is related to larger vacancies, such as vacancy complexes or vacancy clusters. In the current study, because the positron trapping centers must be isolated and negatively charged, they are reasonably attributed to cation vacancies, such as V_{Al} and V_{Lu}, and their related complexes.

From Table III, it can be seen that there was a decrease of τ_1 from 194 ps to 175 ps in as-grown LuYAG:Pr crystals after Li-codoping. The 194 ps component in the as-grown crystal is likely to be related to Al or Lu vacancies given that it is much longer than the bulk lifetime of similar oxides, while the 175 ps component in the Li-codoped sample is closer to the bulk lifetime in YAG [57]. This lifetime could also be a manifestation of the delocalized bulk lifetime and small vacancies that are not separable in the fitting routine. The change of τ_1 towards a bulk lifetime component is a sign of less positron trapping after Li-codoping, which could be associated with the filling of isolated V_{Al} and/or V_{Lu} vacancies by Li ions. Meanwhile, τ_2 remained almost identical. In YAG:Ce crystals grown under O-poor condition, a positron lifetime τ_2 of 305 ps was ascribed to the complex defects in which oxygen vacancies are next to Al vacancies because cation and anion vacancies tend to cluster together due to their positive binding energy [57,58]. Therefore, the slightly longer τ_2 in the non-codoped LuYAG:Pr crystal can be ascribed to the V_O related complex defects.

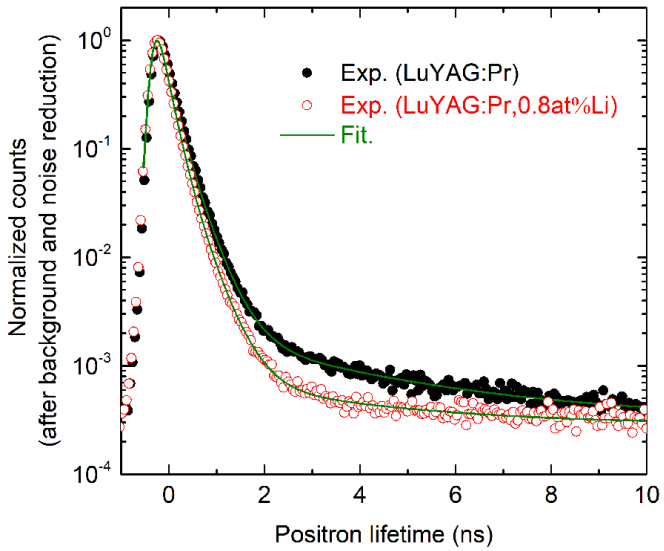

FIG. 11 The PALS spectra of the LuYAG:Pr and LuYAG:Pr,Li samples.

TABLE III. PALS analysis results with three-lifetime fitting for LuYAG:Pr and LuYAG:Pr,Li samples. Note that the positron source contributes approximately 15% to the second component, I_2.

Samples	τ_1 (ps)	I_1 (%)	τ_2 (ps)	I_2 (%)	τ_3 (ns)	I_3 (%)	Fitting Variance
LuYAG:Pr	194±4	69±2	377±9	29±2	3.19±0.09	1.41±0.03	1.17
LuYAG:Pr,Li	175±2	80±1	376±8	20±1	3.10±0.20	0.46±0.02	1.01

IV. Conclusions

The absolute light yield and gamma-ray energy resolution of 10 mm×10 mm×10 mm LuYAG:Pr single crystals are enhanced from 15,600 to 24,800 photons/MeV, and 5.3 to 4.3% at 662 keV, respectively, by Li co-doping. Li codoping does not induce the conversion of stable Pr^{3+} to Pr^{4+}. The Li ions are found to occupy multiple sites, but dominantly at the 4-fold interstitial sites and 4-fold Al sites. The native acceptor defects, such as isolated

V_{Lu}^{3-} and V_{Al}^{3-} vacancies, are expected to be reduced by the filling of Li codopants. Compared to V_{Lu}^{3-} and V_{Al}^{3-}, Li_{Al}^{2-} and Li_{Lu}^{2-} are less attractive to holes due to the lower charge state, which leads to lower hole trapping cross sections and shallower hole trapping levels. Thus, lowering the hole trapping energy and cross sections by codoping with Li may increase the probability of hole trapping by Pr^{3+} and enhances the light yield. Such a study is crucial for understanding the critical role of Li^{+} in improving garnet scintillators, and even oxide scintillators in common.

ACKNOWLEDGEMENTS

This work is supported by Siemens Medical Solutions and the Tennessee Higher Education Commission. This work is partially supported by the Fujian Institute of Innovation, Chinese Academy of Sciences (Grant No. FJCXY18040202), and Youth Innovation Promotion Association funded by Chinese Academy of Sciences. M.H.D. was supported by the U. S. Department of Energy, Office of Science, Basic Energy Sciences, Materials Sciences and Engineering Division. D.H. and S.C. were supported by the State Scholarship Fund in China and CC of ECNU.

REFERENCES

[1] Dujardin, C.; Auffray, E.; Bourret, E.; Dorenbos, P.; Lecoq, P.; Nikl, M.; Vasil'ev, A. N.; Yoshikawa, A.; Zhu, R., Needs, trends and advances in inorganic scintillators, IEEE Trans. Nucl. Sci. **65**, 1977 (2018).

[2] Hofstadter, R., Alkali halide scintillation counters, Phys. Rev. **74**, 100 (1948).

[3] Loef, E. V. D. van; Dorenbos, P.; and Eijk, C. W. E. van, High-energy-resolution scintillator: Ce^{3+} activated $LaBr_3$, Appl. Phys. Lett. **79**, 1573 (2001).

[4] Cherepy, N. J.; Hull, G.; Drobshoff, A. D.; Payne, S. A.; van Loef, E.; Wilson, C. M.; Shah, K.; Roy, U. N.; Burger, A.; Boatner, L. A.; Choong, W.-S.; Moses, W. W., Strontium and barium iodide high light yield scintillators. Appl. Phys. Lett. **92**, 083508 (2008).

[5] Stand, L.; Zhuravleva, M.; Lindsey, A.; and Melcher, C. L., Growth and characterization of potassium strontium iodide: A new high light yield scintillator with 2.4% energy resolution, Nucl. Instrum. Methods Phys. Res., Sect. A **780**, 40 (2015).

[6] Lindsey, A. C.; Zhuravleva, M.; Stand, L.; Wu, Y.; and Melcher, C. L., Crystal growth and characterization of europium doped $KCaI_3$, a high light yield scintillator, Opt. Mater. **48**, 1 (2015).

[7] Wu, Y.; Li, Q.; Chakoumakos, B. C.; Zhuravleva, M.; Lindsey, A. C.; Johnson II, J. A.; Stand, L.; Koschan, M.; and Melcher, C. L., Quaternary iodide $K(Ca,Sr)I_3:Eu^{2+}$ single-crystal scintillators for radiation detection: crystal structure, electronic structure, and optical and scintillation properties, Adv. Opt. Mater. **4**, 1518 (2016).

[8] Johnson, J. A.; Zhuravleva, M.; Stand, L.; Chakoumakos, B. C.; Wu, Y.; Greely, I.; Rutstrom, D.; Koschan, M.; and Melcher, C. L., Discovery of new compounds and scintillators of the A_4BX_6 family: crystal structure, thermal, optical, and scintillation properties, Cryst. Growth Des. **18**, 5220 (2018).

[9] Wu, Y.; Han, D.; Chakoumakos, B. C.; Shi, H.; Chen, S.; Du, M. H.; Greeley, I.; Loyd, M.; Rutstrom, D.; Stand, L.; Koschan, M.; and Melcher, C. L., Zero-dimensional Cs_4EuX_6 (X=Br, I) all-inorganic perovskite single crystals for gamma-ray spectroscopy, J. Mater. Chem. C **6**, 6647 (2018).

[10] Dorenbos, P., Fundamental limitations in the performance of Ce^{3+}-, Pr^{3+}-, and Eu^{2+}-activated scintillators, IEEE Trans. on Nucl. Sci. **57**, 1162 (2010).

[11] Li, Q.; Grim, J. Q.; Ucer, K. B.; Burger, A.; Bizarri, G. A.; Moses, W. W.; and Williams, R. T., Host structure dependence of light yield and proportionality in scintillators in terms of hot and thermalized carrier transport, Phys. Status Solidi RRL **6**, 346 (2012).

[12] Grim, J. Q.; Li, Q.; Ucer, K. B.; Burger, A.; Bizarri, G. A.; Moses, W. W.; and Williams, R. T., The roles of thermalized and hot carrier diffusion in determining light yield and proportionality of scintillators, Phys. Status Solidi A **209**, 2421 (2012).

[13] Moses, W. W.; Payne, S. A.; Choong, W.-S.; Hull, G.; and Reutter, B. W., Scintillator non-proportionality: present understanding and future challenges, IEEE Trans. Nucl. Sci. **55**, 1049 (2008).

[14] Khodyuk, I. V., Nonproportionality of inorganic scintillators, doctoral thesis, Uitgeverij BOXPress, 2013.

[15] Kamada, K.; Endo, T.; Tsutumi, K.; Yanagida, T.; Fujimoto, Y.; Fukabori, A.; Yoshikawa, A.; Pejchal, J.; and Nikl, M., Composition-engineering in cerium-doped $(Lu,Gd)_3(Ga,Al)_5O_{12}$ single-crystal scintillators, Cryst. Growth Des. **11**, 4484 (2011).

[16] Spurrier, M.; Szupryczynski, P.; Yang, K.; Carey, A.; and Melcher, C. L., Effects of Ca^{2+} co-doping on the scintillation properties of LSO:Ce, IEEE Trans. Nucl. Sci. **55**, 1178 (2008).

[17] Alekhin, M. S.; Haas, J. T. M. de; Khodyuk, I. V.; Krämer, K. W.; Menge, P. R.; Ouspenski, V.; and Dorenbos, P., Improvement of γ-ray energy resolution of $LaBr_3:Ce^{3+}$ scintillation detectors by Sr^{2+} and Ca^{2+} co-doping, Appl. Phys. Lett. **102**, 161915 (2013).

[18] Wu, Y.; Li, Q.; Rutstrom, D. J.; Greeley, I.; Stand, L.; Loyd, M.; Koschan, M.; and Melcher, C. L., Effects of zirconium codoping on the optical and scintillation properties of $SrI_2:Eu^{2+}$ single crystals, Nucl. Instrum. Methods Phys. Res., Sect. A DOI:10.1016/j.nima.2018.09.077.

[19] Moszynski, M.; Kapusta, M.; Mayhugh, M.; Wolski, D.; and Flyckt, S. O., Absolute light output of scintillators, IEEE Trans. Nucl. Sci. **44**, 1052 (1997).

[20] Kapusta, M.; Balcerzyk, M.; Moszyński, M.; and Pawelke, J., A high-energy resolution observed from a YAP:Ce scintillator, IEEE Trans. Nucl. Sci. **421**, 610 (1999).

[21] Foster, C.; Wu, Y.; Koschan, M.; and Melcher, C. L., Improvements in light yield and energy resolution by Li^+ codoping $(Lu_{0.75}Y_{0.25})_3Al_5O_{12}:Pr^{3+}$ single crystal scintillators, Phys. Status Solidi RRL **12**, 1800280 (2018).

[22] Liu, S.; Mares, J. A.; Feng, X.; Vedda, A.; Fasoli, M.; Shi, Y.; Kou, H.; Beitlerova, A.; Wu, L.; D'Ambrosio, C.; Pan, Y.; and Nikl, M., Towards bright and fast $Lu_3Al_5O_{12}$:Ce,Mg optical ceramics scintillators, Adv. Opt. Mater. **4**, 731 (2016).

[23] Kamada, K.; Yanagida, T.; Endo, T.; Tsutumi, K.; Usuki, Y.; Nikl, M.; Fujimoto, Y.; Fukabori, A.; and Yoshikawa, A., 2 inch diameter single crystal growth and scintillation properties of Ce:$Gd_3Al_2Ga_3O_{12}$, J. Cryst. Growth **352**, 88 (2012).

[24] Drozdowski, W.; Brylew, K.; Wojtowicz, A. J.; Kisielewski, J.; Świrkowicz, M.; Łukasiewicz, T.; Haas, J. T.M. de; and Dorenbos, P., 33000 photons per MeV from mixed $(Lu_{0.75}Y_{0.25})_3Al_5O_{12}$:Pr scintillator crystals, Opt. Mater. Exp. **4**, 1207 (2014).

[25] Sibczynski, P.; Iwanowska-Hanke, J.; Moszyński, M.; Swiderski, L.; Szawłowski, M.; Grodzicka, M.; Szczęśniak, T.; Kamada, K.; and Yoshikawa, A., Characterization of GAGG:Ce scintillators with various Al-to-Ga ratio, Nucl. Instrum. Methods Phys. Res., Sect. A **772**, 112 (2015).

[26] Wu, Y.; Koschan, M.; Li, Q,; Greelay, I.; and Melcher, C. L., Revealing the role of calcium codoping on optical and scintillation homogeneity in Lu_2SiO_5:Ce single crystals, J. Cryst. Growth **498**, 362 (2018).

[27] Syntfeld-Każuch, A.; Moszyński, M.; Świderski, Ł.; Szczęśniak, T.; Nassalski, A.; Melcher, C. L.; Spurrier, M. A.; Goliszek, B.; Kamiński, P.; and Nowaczyk, M., Energy resolution of Calcium Co-doped LSO:Ce scintillators, IEEE Trans. Nucl. Sci. **56**, 2972 (2009).

[28] Wu, Y.; Tian, M.; Peng, J.; Koschan, M.; Greeley, I.; Foster, C.; and Melcher, C. L., On the role of Li codoping in simultaneous improvement of light yield, decay time and afterglow of $Lu_2SiO_5:Ce^{3+}$ scintillation detectors, Phys. Status Solidi RRL **13**, 1800472 (2019).

[29] Wu, Y.; Peng, J.; Rutstrom, D.; Koschan, M.; Foster, C.; and Melcher, C. L., Unravelling the critical role of site occupancy of lithium codopants in $Lu_2SiO_5:Ce^{3+}$ single-crystalline scintillators, ACS Appl. Mater. Interface **11**, 8194 (2019).

[30] Dickens, P. T.; Haven, D. T.; Friedrich, S.; Saleh, M.; and Lynn, K. G.; Increased luminescence and improved decay kinetics in lithium and cerium co-doped yttrium aluminum garnet scintillators grown by the Czochralski method, J. Appl. Phys. **121**, 123104 (2017).

[31] Liu, S.; Feng, X.; Mares, J. A.; Babin, V.; Hu, C.; Kou, H.; D'Ambrosio, C.; Li, J.; Pan, Y.; and Nikl, M., Effects of Li^+ ions co-doping on luminescence, scintillation properties and defects characteristics of LuAG:Ce ceramics, Opt. Mater. **64**, 245 (2017).

[32] Derdzyan, M. V.; Hovhannesyan, K. L.; Yeganyan, A. V.; Sargsyan, R. V.; Novikov, A.; Petrosayn, A. G.; and Dujardin, C., Dissimilar behavior of YAG:Ce and LuAG:Ce scintillator garnets regarding Li^+ co-doping, CrystEngComm **20**, 1520 (2018).

[33] Liu, S.; Feng, X.; Zhou, Z.; Nikl, M.; Shi, Y.; and Pan, Y., Effect of Mg^{2+} co-doping on the scintillation performance of LuAG:Ce ceramics, Phys. Status Solidi RRL **8**, 105 (2014).

[34] Kamada, K.; Nikl, M.; Kurosawa, S.; Beitlerova, A.; Nagura, A.; Shoji, Y.; Pejchal, J.; Ohashi, Y.; Yokota, Y.; and Yoshikawa, A., Co-doping effects on luminescence and scintillation properties of Ce doped $Lu_3Al_5O_{12}$ scintillator, Nucl. Instrum. Methods Phys. Res A **782**, 9 (2015).

[35] Hohenberg, P.; Kohn, W., Inhomogeneous electron gas. Phys. Rev. **136**, B864 (1964).

[36] Kohn, W.; Sham, L. J., Self-consistent equations including exchange and correlation effects. Phys. Rev. **140**, A1133 (1965).

[37] Kresse, G.; Furthmuller, J., Efficient iterative schemes for ab initio total-energy calculations using a plane-wave basis set. Phys. Rev. B **54**, 11169 (1996).

[38] Kresse, G.; Joubert, D., From ultrasoft pseudopotentials to the projector augmented-wave method. Phys. Rev. B **59**, 1758 (1999).

[39] Perdew, J. P.; Burke, K.; Ernzerhof, M., Generalized gradient approximation made simple. Phys. Rev. Lett. **77**, 3865 (1996).

[40] Euler, F.; Bruce, J. A., Oxygen coordinates of compounds with garnet structure. Acta Crystallographica **19**, 971 (1965).

[41] Lany, S.; Zunger, A., Assessment of correction methods for the band-gap problem and for finite-size effects in supercell defect calculations: Case studies for ZnO and GaAs. Phys. Rev. B **78**, 235104 (2008).

[42] Pejchal, J.; Buryi, M.; Babin, V.; Prusa, P.; Beitlerova, A.; Barta, J.; Havlak, L.; Kamada, K.; Yoshikawa, A.; Laguta, V.; and Nikl, M. Luminescence and scintillation properties of Mg-codoped LuAG:Pr single crystals annealed in air, J. Lumin. **181**, 277 (2017).

[43] Zhuravleva, M.; Friedrich, S.; and Melcher, C. L. Praseodymium valence determination in Lu_2SiO_5, Y_2SiO_5, and $Lu_3Al_5O_{12}$ scintillators by x-ray absorption spectroscopy, Appl. Phys. Lett. **101**, 101902 (2012).

[44] Hu, C.; Feng, X.; Li, J.; Vedda, A.; Ding, D.; Zhou, Z.; Kou, H.; and Pan, Y. Role of Y admixture in $(Lu_{1-x}Y_x)_3Al_5O_{12}$:Pr ceramic scintillators free of host luminescence, Phys. Rev. Appl. **6**, 064026 (2016).

[45] Wu, Y.; Peng, J.; Rutstrom, D.; Koschan, M.; Foster, C.; Melcher, C. L. Unraveling the critical role of site occupancy of lithium codopants in $Lu_2SiO_5:Ce^{3+}$ single-crystalline scintillators, ACS Appl. Mater. Interfaces **11**, 8194 (2019).

[46] Zhao, M.; Xia, Z.; Huang, X.; Ning, L.; Gautier, R.; Molokeev, M. S.; Zhou, Y.; Chuang, Y.; Zhang, Q.; Liu, Q.; and Poeppelmeier, K. R. Li substituent tuning of LED phosphors with enhanced efficiency, tunable photoluminescence, and improved thermal stability, Sci. Adv. **5**, eaav0369 (2019).

[47] Zhu, J.; Gu, M.; Liu, X.; Liu, B.; Huang, S.; Ni, C. First-principles study on stability of Li, Na, Ca in Lu_2SiO_5, J. Lumin. **139**, 1 (2013).

[48] Xu, Z.; Stebbins, J. F. ^{6}Li nuclear magnetic resonance chemical shifts, coordination number and relaxation in crystalline and glassy silicates, Solid State Nucl. Magn. Reson. **5**, 103 (1995).

[49] Choi, M.; Matsunaga, K.; Oba, F.; and Tanaka, I. ^{27}Al NMR chemical shifts in oxide crystals: A first-principles study, J. Phys. Chem. C **113**, 3869 (2009).

[50] Nikl, M.; Vedda, A.; Fasoli, M.; Fontana, I.; Laguta, V. V.; Mihokova, E.; Pejchal, J.; Rosa, J.; and Nejezchleb, K. Shallow traps and radiative recombination processes in $Lu_3Al_5O_{12}$:Ce single crystal scintillator, Phys. Rev. B **76**, 195121 (2007).

[51] McKeever, S. W. S. Thermoluminescence of Solids (Cambridge University Press, Cambridge, England, 1985).

[52] Nikl, M.; Mihóková, E.; Pejchal, J.; Vedda, A.; Zorenko, Y.; and Nejezchleb, K. The antisite LuAl defect-related trap in $Lu_3Al_5O_{12}$:Ce single crystal, Phys. Status Solidi B **242**, R119 (2005).

[53] Springis, M.; Pujats, A.; and Valbis, J. Polarization of luminescence of color-centers in YAG crystals, J. Phys. Condensed Matter **3**, 5457 (1991).

[54**]** Pujats A.; and Spingis, M. The F-type centres in YAG crystals, Radiation effects and defects in solids, **155**, 65 (2001).

[55] Drozdowski, W.; Brylew, K.; Chruscinska, A.; Kamada, K.; Yanagida, T.; and Yoshikawa, A. Scintillation yield enhancement in LuAG:Pr crystals following thermal annealing, Opt. Mater. **34**, 1975 (2012).

[56] Petrosyan, A. G.; Ovanesyan, K. L.; Sargsyan, R. V.; Shirinyan, G. O.; Abler, D.; Auffray, E.; Lecoq, P.; Dujardin, C.; and Pedrini, C. Bridgman growth and site occupation in LuAG:Ce scintillation crystals, J. Cryst. Growth **312**, 3136 (2010).

[57] Selim, F. A.; Varney, C. R.; Tarun, M. C.; Rowe, M. C.; Collins, G. S.; and McCluskey, M. D. Positron lifetime measurements of hydrogen passivation of cation vacancies in yttrium aluminum oxide garnets, Phys. Rev. B **88**, 174102 (2013).

[58] Selim, F. A.; Solodovnikov, D.; Weber, M. H.; and Lynn, K. G. Identification of defects in $Y_3Al_5O_{12}$ crystals by positron annihilation spectroscopy, Appl. Phys. Lett. **91**, 104105 (2007).